NEOPLASIA
www.neoplasia.com

## Original Research

# Noninvasive optoacoustic microangiography reveals dose and size dependency of radiation-induced deep tumor vasculature remodeling

Anna Orlova [a,*]; Ksenia Pavlova [a,b]; Aleksey Kurnikov [a]; Anna Maslennikova [a,b,c]; Marina Myagcheva [d]; Evgeniy Zakharov [d]; Dmitry Skamnitskiy [e]; Valeria Perekatova [a]; Alexander Khilov [a]; Andrey Kovalchuk [a]; Alexander Moiseev [a]; Ilya Turchin [a]; Daniel Razansky [f,g]; Pavel Subochev [a]

[a] Division of Nonlinear Dynamics and Optics, Institute of Applied Physics of Russian Academy of Sciences, 46 Ul'yanov Street, Nizhny Novgorod 603950, Russia
[b] Department of Biophysics, Lobachevsky State University of Nizhny Novgorod, Nizhny Novgorod, Russia
[c] Department of Oncology, Radiation Therapy and Radiology, Privolzhsky Medical Research University, Nizhny Novgorod, Russia
[d] Pathology Department, Nizhny Novgorod Regional Children's Clinical Hospital, Nizhny Novgorod, Russia
[e] Radiotherapy Department, Nizhny Novgorod Regional Oncology Hospital, Nizhny Novgorod, Russia
[f] Institute for Biomedical Engineering and Institute of Pharmacology and Toxicology, Faculty of Medicine, University of Zurich, Zurich, Switzerland
[g] Department of Information Technology and Electrical Engineering, Institute for Biomedical Engineering, ETH Zurich, Zurich, Switzerland

## Abstract

Tumor microvascular responses may provide a sensitive readout indicative of radiation therapy efficacy, its time course and dose dependencies. However, direct high-resolution observation and longitudinal monitoring of large-scale microvascular remodeling in deep tissues remained challenging with the conventional microscopy approaches.

We report on a non-invasive longitudinal study of morphological and functional neovascular responses by means of scanning optoacoustic (OA) microangiography. *In vivo* imaging of CT26 tumor response to a single irradiation at varying dose (6, 12, and 18 Gy) has been performed over ten days following treatment. Tumor oxygenation levels were further estimated using diffuse optical spectroscopy (DOS) with a contact fiber probe.

OA revealed the formation of extended vascular structures on the whole tumor scale during its proliferation, whereas only short fragmented vascular regions were identified following irradiation. On the first day post treatment, a decrease in the density of small (capillary-sized) and medium-sized vessels was revealed, accompanied by an increase in their fragmentation. Larger vessels exhibited an increase in their density accompanied by a decline in the number of vascular segments. Short-lasting response has been observed after 6 and 12 Gy irradiations, whereas 18 Gy treatment resulted in prolonged responses, up to the tenth day after irradiation. DOS

measurements further revealed a delayed increase of tumor oxygenation levels for 18 Gy irradiations, commencing on the sixth day post treatment. The ameliorated oxygenation is attributed to diminished oxygen consumption by inhibited tumor cells but not to the elevation of oxygen supply.

This work is the first to demonstrate the differential (size-dependent) nature of vascular responses to radiation treatments at varying doses *in vivo*. The OA approach thus facilitates the study of radiation-induced vascular changes in an unperturbed *in vivo* environment while enabling deep tissue high-resolution observations at the whole tumor scale.

*Neoplasia (2022) 26, 100778*

# Introduction

Changes in tumor blood supply in response to exposure to ionizing radiation have been a subject of scientific investigations since 1930s [1]. Numerous studies have demonstrated variations of the tumor vascular bed response to irradiation, depending on the total and single dose, fractionation, as well as the histological structure and size of the tumor node [2,3]. The main manifestations of the microvascular response to irradiation are drop of perfusion, elevated permeability of the vascular wall, diminished number of functioning vessels, reduced density of the vascular network, vasoconstriction and decrease in the blood flow velocity [1,4].

Most studies to date have considered the effects on tumor vessels induced by a single irradiation over a wide range of doses [1]. In recent years, in connection with the development of precision irradiation techniques, the main trend in radiation therapy has become the use of higher single doses in one or few fractions (stereotaxic radiotherapy or stereotactic radiosurgery) [5]. Studies on tumor models have shown that irradiation with higher doses leads to significant damage to microcirculation, changes in the tumor microenvironment and subsequent cell death [6].

Investigating the mechanisms underlying tumor tissue destruction by high-dose irradiations, in particular its microvascular responses, is paramount for optimal treatment planning, prognosis and follow-up. One pivotal question is how the different components of tumor vascular bed contribute to the changes in the tumor oxygen state at various time point after exposure to various doses of radiation.

The spatial resolution of traditional contrast-based computed tomography [7] and magnetic resonance imaging [8] methods are inadequate for visualizing the capillary network *in vivo*. Alternatively, various intravital optical microscopy approaches [9–11] can be used for high-resolution angiography with the caveat of having poor penetration depth and small field of view, which limits most studies to superficial observations on a sub-millimeter scale. Doppler ultrasound imaging has an appropriate penetration depth but suffers from insufficient contrast and spatial resolution [12], making it incapable of clearly discerning small vessels having a slow blood flow [13].

The optoacoustic (OA) method is based upon the physical phenomenon of conversion of absorbed light into acoustic waves, which allows for label-free imaging of hemoglobin-containing structures with high optical contrast and much deeper penetration compared to optical microscopy [14]. To this end, OA angiography has been successfully employed for analyzing vascular pattern changes in response to anti-angiogenic therapies [15,16]. A number of OA works have monitored the tumor functional state following radiation therapy (RT) at the macroscopic scale [17–19] by identifying radiation-induced changes in blood oxygen saturation averaged through thick 2D cross-sections. Radiation-induced structural changes of the cortical and skull microvasculature were also studied with optical-resolution OA microscopy

[20], albeit the study was limited to healthy tissues exposed to radiation and effective penetration well below 1mm.

Most OA imaging systems have been implemented with piezocomposite sensors that typically exhibit a limited bandwidth around their central resonant frequency [21,22]. However, unequivocal differentiation between vascular structures of various sizes implies detection of OA responses over a broad range of frequencies [23]. An ultrawideband optoacoustic angiography can be enabled through the use of non-resonant piezopolymer materials based on polyvinidylene fluoride (PVDF) [24], which was previously established for scanning OA angiography in the visible and IR range of optical wavelengths [25].

In this work, we utilized PVDF-based acoustic-resolution OA microscopy system [26] for monitoring the response of tumor vascular network to single exposures to varying doses of ionizing radiation. By employing a murine colon carcinoma CT26 model, we demonstrate, for the first time, the differential (size-dependent) nature of vascular responses to RT *in vivo*. DOS measurements were further employed to monitor tumor oxygenation levels using a contact fiber-optic probe.

# Methods and materials

## *Animals and tumor models*

The experiments were carried out on eighteen 6-week-old female Balb/c mice (18–20 g). The animals were obtained from the "Pushchino" Nursery for laboratory animals (Moscow, Russia). The study was performed on the model of murine colon carcinoma CT26 (ATCC No CRL-2638). $5 \times 10^5$ cells in 50 $\mu$l PBS were injected subcutaneously into the outer side of the left thigh.

The experiments were conducted in accordance with the codes and enactments regulating research studies pertaining the safety and efficiency of pharmaceuticals (Regulation by Ministry of Health and Social Development of Russian Federation No. 708-n from 23.08.2010), as well as international legal and ethical rules pertaining experimental use of animals (NIH Publications No. 8023, revised, 1978). The animal studies were approved by the Ethics Committee of Lobachevsky State University of Nizhny Novgorod (Protocol No 47, 22.10.2020).

## *OA imaging system and data processing*

Detailed description of the raster-scan optoacoustic angiography apparatus is available elsewhere [26,27]. In short, the generated OA responses were captured by a single-element spherically focused ultrasonic detector based on 9 $\mu$m polyvinylidene fluoride (PVDF) film. The transducer had an ultrawideband detection bandwidth between 1 and 100 MHz, F = 6.8 mm focal distance and 0.6 numerical aperture. The scanning OA head was
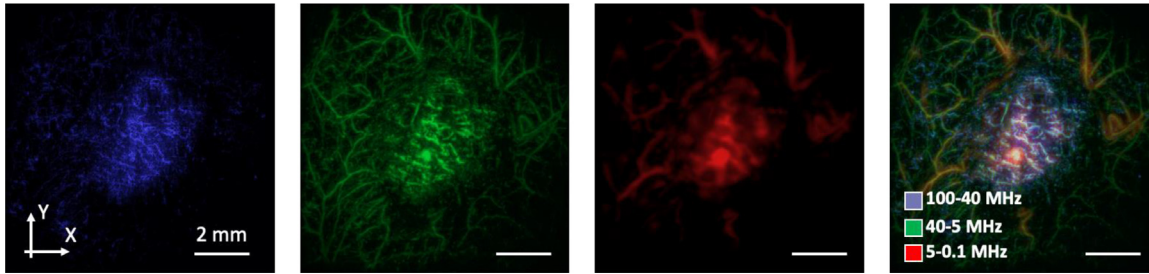
**Figure 1.** MIP OA images of CT26 tumor reconstructed in three frequency ranges and merged: 100–40 MHz range (small vessels of <40 $\mu$m in diameter); 40–5 MHz range (vessels of middle sizes of 40–300 $\mu$m in diameter); 5–0.1 MHz range (large structures of >300 $\mu$m in diameter).

mounted on two computer-driven stages M-664 and LS-40 (PI, Germany) performing fixed lateral steps ($\delta x = \delta y = 15$ $\mu$m) within lateral scanning areas ($\Delta X = \Delta Y = 10$ mm). The low-jitter input of the laser Wedge HB 532 (BrightSolutions, Italy) was triggered by the scanning stages and provided optical pulses at a 532 nm wavelength (close to isosbestic point for hemoglobin) with 1.4 ns pulse duration and 300 $\mu$J per-pulse energy. The average radiant exposure at the tumor surface was less than 4 mJ/cm$^2$ complying with the ANSI Z136.1 standard for laser safety. Two-channel 16-bit analog-to-digital converter (ADC) CSE1622 (Gage, USA) with 200 MS/s was triggered by the laser pulses, thus capturing single OA waveforms (A-scans) corresponding to discrete XY positions of the scanning head.

After the acquisition of OA data, an acoustic reconstruction algorithm [28] was consequently applied to the lateral scans. Images were reconstructed separately in three frequency ranges [15,29,30] (5–0.1 MHz, 40–5 MHz, 100–40 MHz) corresponding to the characteristic dimensions of blood-containing objects in the 0.3–15 mm, 40–300 μm, 15–40 μm ranges when assuming 1.5 mm/μs sound speed. Note, however, that spectral content of OA waveforms generated by each vessel generally depends on multiple physical and geometrical parameters related to the propagation medium, vessel orientation, ultrasonic detector geometry etc. The OA angiograms corresponding to different frequencies were subsequently color-coded using Avizo software (Thermo Scientific, USA) and plotted as maximum intensity projections (MIP) (Fig. 1).

Each MIP image was then binarized and analyzed using "Color Threshold and Analyze Particles" ImageJ plugin (NIH, USA). For the vessel analysis tumor zones free from superficial scabs were selected, at the outer boundary of the peripheral small vessel area. Threshold parameter was chosen to reduce the amount of background noise in binarized OA images. Vascular density was determined as a percentage of tumor area occupied by vessels in the OA images. Number of vessel segments was calculated as a ratio between the number of visualized vessel fragments and the corresponding vessel area. The characteristic size of vessel segments was calculated by averaging all the vessel thicknesses.

### Diffuse optical spectroscopy

The DOS studies were carried out using a fiber-optic-based system operated in a reflectance mode with a broadband LED source (MCWHF2, Thorlabs Inc., USA) used for illumination and a spectrometer (QE65000, Ocean Optics Inc., USA) as a detector. The probe includes four 200 μm optical fibers (Polironik LLC, Russia) with a fixed separation of 1.75 mm between them [27,31]. The intensity of scattered light at two different source-detector separations was measured and used for reconstructing the absorption spectra in the 520–590 nm wavelength range, while hemoglobin concentration and blood oxygen saturation (StO$_2$) were calculated using a deep learning neural network [32]. For DOS investigation the contact surface of the optical probe was placed on the tumor region.

For the current DOS configuration (source-detector separation of 1.75–3.5 mm and spectral range 500–600 nm), the median probing depth is about 1–2 mm according to Monte-Carlo simulation results. Thus, DOS results predominantly associated with the average hemoglobin concentrations in subcutaneous tumor tissue were considered. Between 3 and 5 diffuse optical spectra were measured from the surface of each tumor.

### Irradiation and measurement protocol

Irradiation was performed with Novalis Tx linear electron accelerator (Varian Medical Systems, USA) in the 6X SRS mode with an equalizing filter, the source to surface distance 100 cm and the average dose rate 1000 MU/min at a target depth. Treatment was delivered with a multi-leaf collimator to form an irradiation field of $10 \times 10$ mm, the size of the field of the accelerator shutters was $22 \times 22$ mm. Since the tumor was located under the skin, a 13-mm thick thermoplastic bolus was used to create a uniform irradiation area.

Animals (4–5 mice in a group) were irradiated at the single doses of 6, 12 and 18 Gy. Four mice were used as an untreated control. Irradiation was performed on the 7th day of tumor growth (Fig. 2A) when the tumor diameter reached 5–7 mm. Prior to irradiation, mice were anesthetized with intramuscular injection of the mixture of 40 mg/kg Zoletil (Valdepharm, France) and 10 mg/kg XylaVet (Alpha-Vet Veterinary Ltd., Hungary).

OA and DOS investigations were performed every 2–3 days for 11 days starting from the 6th day after tumor inoculation (one day prior to RT). For the study, the animals were anesthetized with 1.5% isoflurane (Karizoo Laboratories, Spain) in 100% oxygen with a flow of 0.1 l/min and fixed on a support plate in a side position. For OA angiography the center of the tumor was aligned with the center of the scanned area, while the focal position of ultrasonic detector was targeted at 500 $\mu$m depth from the skin surface. The measurement volume was similar for all the frequency ranges covering the approximately 400 $\mu$m thick skin [33,34] and the superficial layer of the tumor up to a depth of about 1 mm.

Before each OA/DOS investigation, tumors were measured along three perpendicular directions with a caliper, and their volumes were calculated as follows: $V = (4/3) \times \pi \times (a/2) \times (b/2) \times (c/2)$, where V is the volume and a, b and c are the three corresponding diameters. The tumor growth inhibition factor was defined as (1—(mean V of treated tumors)/(mean V of control tumors)) $\times$ 100% [35].

### Morphological study

Histological examination was performed on the 3rd (one mice per group) and 10th (3–4 mice per group) days after treatment. For tissue fixation, samples were placed into 10% neutral buffered formaldehyde (Biovitrum, Russia) for 24 h. Samples were processed on an automated tissue processor (Logos, Milestone Medical, Italy) with the protocol consisting of incubation
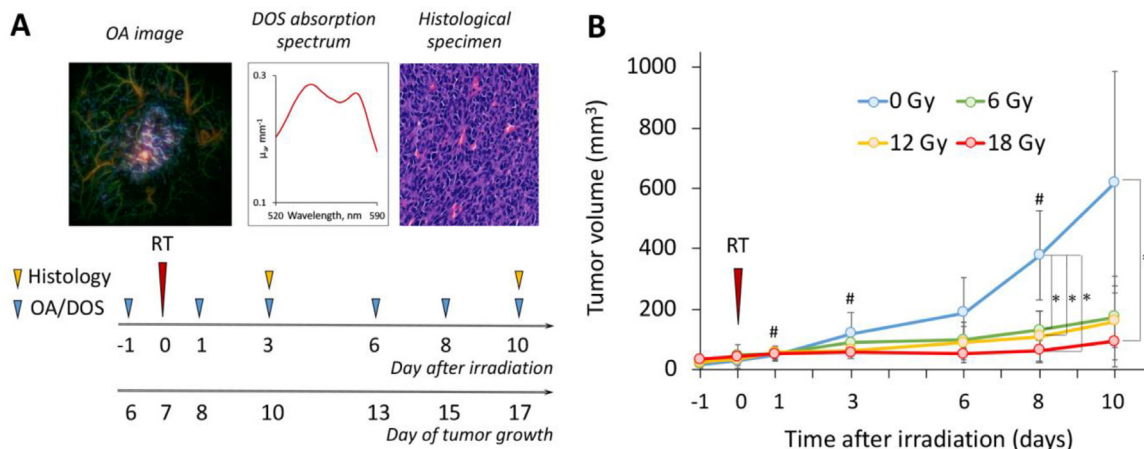
**Figure 2.** Single-dose irradiation inhibits CT26 growth: experiment schedule (A) and dynamics of CT26 volume after irradiation at different doses (B). Time point of tumors irradiation is indicated by red triangle, time points of OA and DOS investigation - by blue triangles, time points of histology – by yellow triangles. * - statistically significant differences between the treatment groups. # - statistically significant differences between the current and the initial values.

in isopropanol for no longer than 10 h at room temperature. The paraffin-embedded tumor samples were cut into 3 μm-thick slices on a rotary microtome (Thermo Fisher Scientific, USA). Deparaffinized slices were manually stained with hematoxylin and eosin (H&E) (Biovitrum, Russia) to assess general tissue architectonics. The tissue slices were scanned using a high-resolution digital slide scanner Pannoramic 250 (3DHistech, Hungary).

In order to quantify the tumor vascularity, we calculated the red blood cell (RBC) fraction consisting of blood vessels and hemorrhages, as the ratio between the erythrocytes-containing areas and the total tumor area in the sections. RBC fraction calculation was performed using the Analyze Particles ImageJ function choosing as a reference the values of brightness, saturation and hue, which coincide with the values of erythrocyte staining for eosin. 5–14 slices per tumor were analyzed.

Mitotic index was calculated as quantity of mitotic figures per 1 mm$^2$.

Immunohistochemical staining with antibodies against Factor VIII-Related Antigen/von Willebrand factor (vWF) (Rabbit polyclonal Antibody, Cell Marque, USA) for endothelial cells, megakaryocytes, platelets and mast cells was performed by manual IHC established protocol (one mouse per group on the 3rd and 10th days after treatment). ICH allows the visualization of vascular structures including those that do not contain red blood cells, such as collapsed vessels and very small newly formed tumor vessels.

### Statistical analysis

All measurement data obtained for tumor growth are shown as means $\pm$ SD; StO$_2$, hemoglobin concentrations are shown as means $\pm$ SEM. Parameters of vascular density, vessels segments number, size and RBC fraction are shown as the box-whisker plots including interquartile ranges, medians, means, minimum and maximum values of the data set. One-way ANOVA with Bonferroni correction was performed to estimate the significance of the differences between treatment groups in each time point and t-test for dependent samples - between the current and initial values inside the groups. Statistically significant value was taken as $p \leq 0.05$.

## Results

### Single-dose irradiation affects the growth of CT26 tumor

Figure 2B shows CT26 tumor growth commencing on day 6th after tumor inoculation. The volume of untreated tumors increased from

$17.7 \pm 11.9$ mm$^3$ to $619.4 \pm 365.5$ mm$^3$ on day 17 (10 days after irradiation).

Irradiated tumors appeared to be of smaller size as compared to untreated ones at the time of monitoring completion. Differences between treated and untreated tumors on 8th day of the experiment were assessed for all groups: 6 Gy ($p = 0.04$), 12 Gy ($p = 0.02$) and 18 Gy ($p < 0.01$). Tumor growth inhibition index was 72% for 6 Gy-irradiated tumors, 74% for 12-Gy irradiated tumors and 85% for tumors irradiated with the 18 Gy dose.

### Irradiation-induced changes of tumor vascular morphology are dependent on the vessels size

As evidenced by the OA images of CT26 tumors before and after irradiation (Fig. 3), the severity and duration of vascular response depended on the vessels size. Upon the start of monitoring, the tumors presented as regions containing small, tortuous, randomly distributed vessels, significantly differing from the normal microvasculature in the surrounding healthy tissues. The characteristic features of untreated CT26 tumors are the formation of lengthened small-sized vessel structures along with the development of extensive hemoglobin-containing regions located on the surface of the neoplasm, subsequently forming a superficial scab in the later stages of tumor development. After irradiation, only short fragmented vascular structures remained in the tumor region accompanied by an overall reduction of tumor vascularity. The most pronounced response occurred for the 18 Gy irradiation dose.

For untreated tumors, no significant changes of density of small and middle-sized vessels were revealed during the monitoring period (Fig. 4A,B). Large vessels exhibited a temporary rise in vascular density (Fig. 4C), which lasted up to day 6 of the experiment.

Furthermore, a rapid decrease in the density of small vessels was observed within one day after irradiation (Fig. 4A). Relative changes from the baseline values were obtained for 12 Gy group ($p < 0.01$) one day following irradiation and for 18 Gy group ($p < 0.05$) at days 1 and 10 post irradiation. Differences with the untreated group were observed for tumors irradiated with 18 Gy at day 3 ($p = 0.02$) and day 6 ($p = 0.03$) after treatment. The drop in the density of middle-sized vessels lasted until day 6 after treatment (Fig. 4B), with the vascular density values dropping at one day post RT by a factor of approximately 2, 1.5, and 3 in the 6, 12, and 18 Gy groups, respectively. On the last day of monitoring the vascular density remained low in the tumors which were irradiated with the 18 Gy dose. Large ($>300 \mu$m) vascular structures manifested an opposite trend in response to irradiation, as evinced
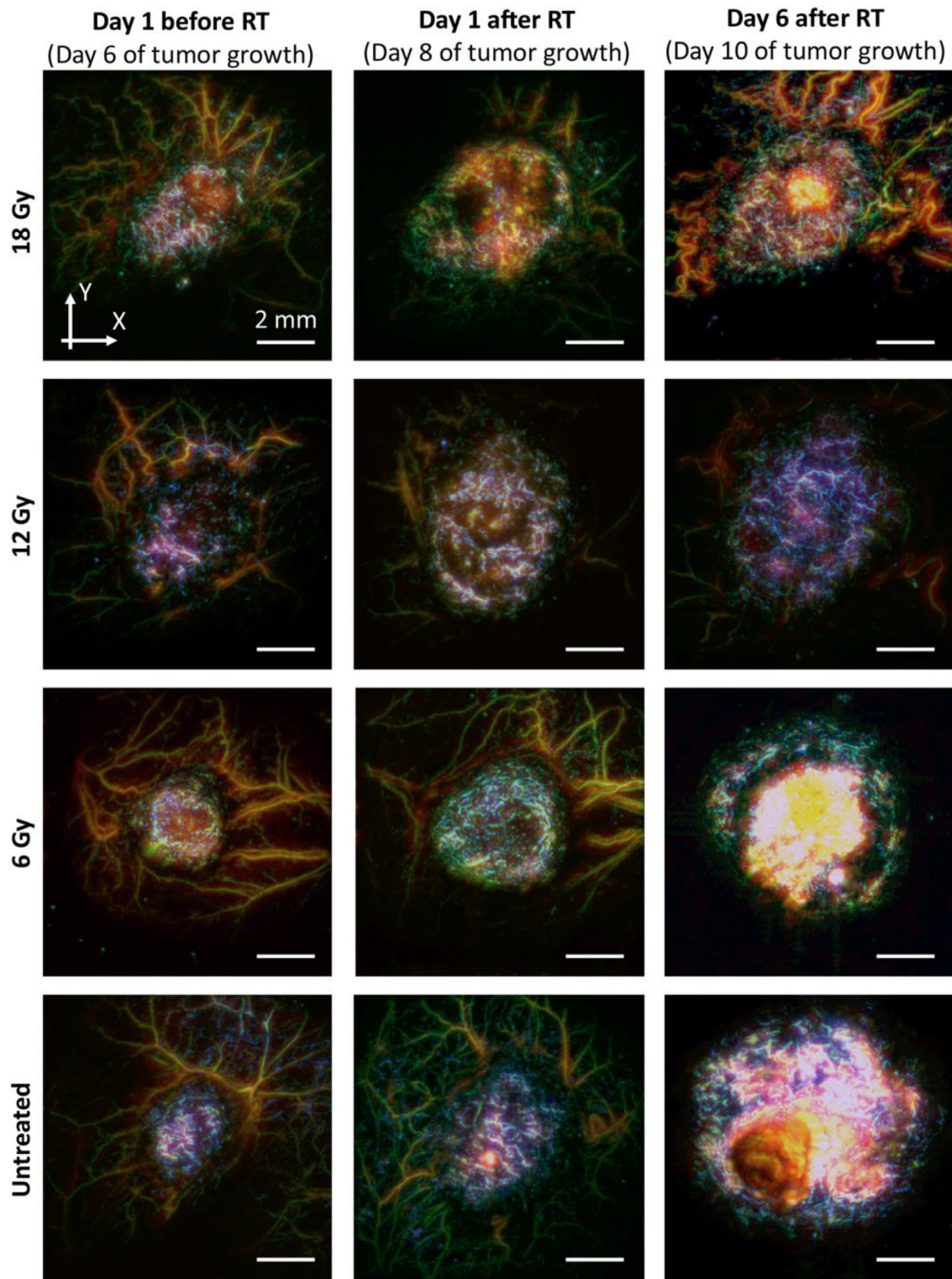
**Figure 3.** Examples of OA images of CT26 vasculature before and after irradiation at different doses. The images were merged through the three ultrasound frequency ranges: blue – 100–40 MHz range (small vessels of <40 $\mu$m in diameter), green – 40–5 MHz range (vessels of middle sizes of 40–300 $\mu$m in diameter) and red – 5–0.1 MHz range (large vessels of >300 $\mu$m in diameter).
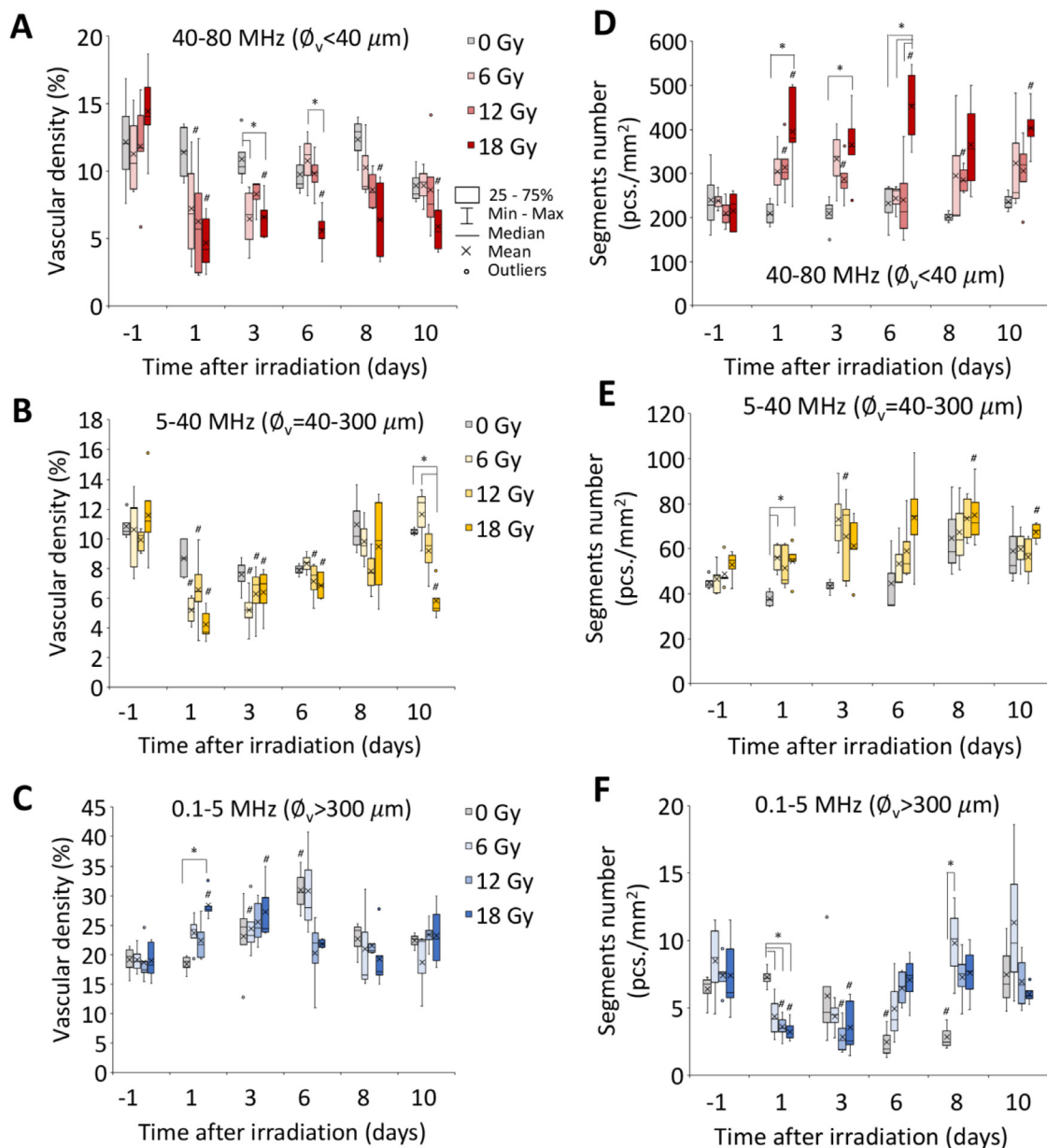
**Figure 4.** Vascular density (A–C) and vessels segments number (D–F) of small (A,D), middle (B,E) and large (C,F) vessels of CT26 tumors after irradiation. $\varnothing_v$ – vessels diameter. * - statistically significant differences between the treatment groups. # - statistically significant differences between the current and the initial values.

by temporary increase in the vessel's density (Fig. 4C). The most pronounced changes were presented by tumors irradiated with 18 Gy at day 1 post RT when the indicator has risen in relation to the baseline ($p < 0.01$) and untreated tumors ($p < 0.01$).

Besides the changes in vascular density, a radiation-induced response was manifested in the structure of the vascular network (Fig. 4D–F). The tumors irradiated with the 6 Gy dose demonstrated a nonsignificant temporary increase in the number of segments of small-sized vessels (Fig. 4D), whereas for tumors irradiated with 12 Gy the increase in the number of small-sized segments was more pronounced. Differences with respect to the baseline were observed at days 1 ($p = 0.03$), 3 ($p = 0.04$) and 8 ($p = 0.02$) after RT. After, the most significant rise in the small-sized vessel segmentation was caused by irradiation with the 18 Gy dose, commencing after day 1 post treatment ($p = 0.04$ as compared to the baseline and $p = 0.02$ as compared to untreated tumors) and sustaining throughout the entire duration of the study. While 18 Gy irradiation caused a persistent drop in the size of vessels segments (Fig.

S1A), the lower doses have only resulted in a temporary decrease followed by recovery to the initial values starting on day 3 after irradiation.

For mid-sized vessels, a similar yet less pronounced trend was observed (Figs. 4E and S1B). Large hemoglobin containing structures demonstrated a decrease in the number of segments (Fig. 4F). Regardless of the exposure dose, the maximum difference between irradiated and non-irradiated tumors was observed on the 1st day after radiation ($p = 0.01$ for 6 Gy, $p < 0.01$ for 12 Gy and 18 Gy), concurrently with an overall increase in the size of large vascular structures (Fig. S1B). For irradiation doses of 12 Gy and 18 Gy, differences were found both in relation to the baseline ($p = 0.02$ and $p < 0.01$, respectively) as well as non-irradiated tumors ($p = 0.04$ and $p = 0.01$, respectively).

*Late increase of blood oxygen saturation after 18 Gy irradiation*

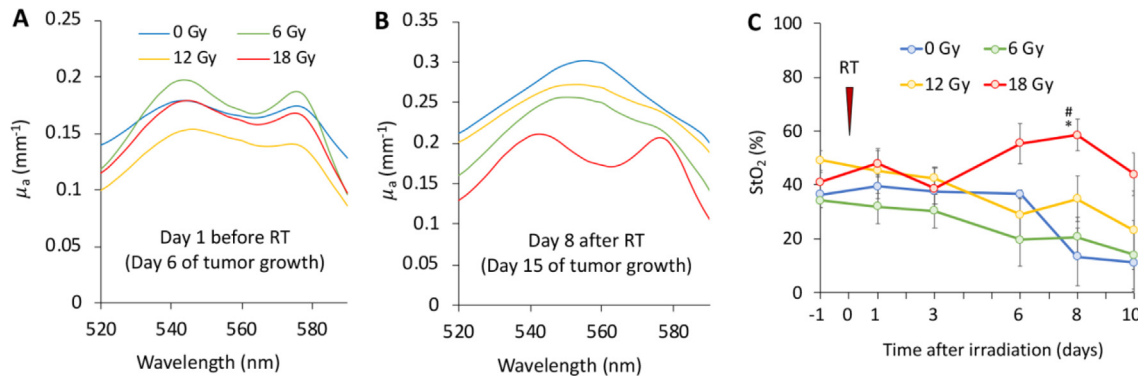DOS shows that RT influences tumor $StO_2$ level.

**Figure 5.** DOS monitoring of CT26 tumors after irradiation: typical reconstructed spectra of absorption coefficient for untreated and treated tumors at 6th (A) and 15th (B) days of tumor growth; blood oxygen saturation level ($StO_2$, C). Time point of tumors irradiation is indicated by red triangle. * - statistically significant differences between the treatment groups. # - statistically significant differences between the current and the initial values.

Examples of the optical absorption coefficient spectra of the CT26 tumor retrieved by DOS on days 6 and 15 after tumor inoculation are shown in Fig. 5, corresponding to 1 day prior to and 8 days post irradiation. Before irradiation the tumor absorption spectra were similar for all the animal groups (Fig. 5A), suggesting similar chromophore content in the tumors. On day 8 of the experiment the non-irradiated tumors as well as the 6 Gy and 12 Gy groups predominantly exhibited deoxyhemoglobin content (Fig. 5B). For tumors irradiated with the 18 Gy, the shape of the absorption spectrum remained unaltered.

Dynamics of $StO_2$ levels calculated from the DOS spectral data are shown in Fig. 5C. Upon start of the monitoring, the average $StO_2$ measured across the CT26 tumor was in the 35–50% range, resembling well the previously reported values for CT26 tumors [36,37]. In untreated tumors $StO_2$ remained unchanged between days 6 and 13 of the monitoring followed by a statistically insignificant decrease. A gradual decrease in the level of $StO_2$ was revealed for tumors exposed to 6 Gy and 12 Gy radiation doses, while no statistically significant variations were detected in non-irradiated tumors. However, tumors treated with the 18 Gy dose demonstrated a delayed increment in the tissue saturation starting from day 6 post treatment. At day 8 after irradiation, the differences became significant as compared to the baseline reading ($p < 0.01$) and untreated tumors ($p = 0.02$).

In tumors irradiated with the 18 Gy dose a temporary decrease in the concentration of deoxyhemoglobin was observed from day 3 to day 10 after irradiation (Fig. S2B). On the other hand, there were no statistically significant differences in the values of oxyhemoglobin ($HbO_2$) and total hemoglobin (tHb) content between the irradiated and untreated groups (Fig. S2A,C).

### Ex vivo *microscopic analysis detected reduction in tumor vascularity*

Histopathological study of H&E-staining samples and ICH study for vWF performed at days 3 and 10 after irradiation (Fig. 6) confirmed the *in vivo* OA findings. Both histology and ICH study have shown reduction in the vascular density. When comparing H&E and anti-vWF stainings, the latter is sensitive to endothelial cells thus was able to reveal more vessel segments due to the ability to visualize vessels not containing erythrocytes (Fig. 6A,B). Large hemorrhagic regions are formed by the 10th day of experiment with their area decreasing after irradiation (Fig. S3). IHC showed the decrease of vessels number after irradiation with only small vessels being present comparable in size with tumor cells after 18 Gy (Fig. 6B).

The RBC-positive areas in H&E images (Fig. 6C) decreased in size at 10 days post irradiation with statistically significant difference for tumors irradiated at 18 Gy as compared to untreated tumors ($p = 0.05$). Mitotic index gradually decreased with increasing radiation dose, however even the maximum drop recorded for the 18 Gy dose was not statistically significant (Fig. 6D).

## Discussion

Detailed insight into radiation-induced tumor microvasculature changes is important for maximizing efficacy of radiotherapy treatments. In particular, study of the mechanisms underlying tumor responses to single high dose irradiation represents an urgent challenge in radiobiology. One key aspect is the dynamic assessment of the delicate interplay between tumor vasculature responses and the inextricably linked changes in oxygen state as well as its contribution to the processes driving the tumor cells death. In this work, we used complementary methods for assessing structure of the tumor neovasculature and oxygenation state under the influence of RT. Scanning OA angiography assisted with an ultrawide detection bandwidth transducer allowed for precision assessment of both micrometer-sized capillaries and millimeter-size vascular structures often co-existing within the same tumor areas [38,39].

Murine colon carcinoma CT26 is characterized by rapid growth and relatively high vascularity [40]. CT26 vessels diameter depends on the phase of tumor growth and varies in the 7–200 $\mu$m range [41]. OA angiography revealed the structural architecture of the CT26 vascular system in the process of tumor growth. Analysis of different ultrasound frequency ranges allowed to observe the formation of elongated small- and mid-sized vascular structures. Vascularization rate fluctuations were similarly noted for the CT26 tumor in previous studies [40,42]. We also observed an expansion of large hemoglobin-containing zones, which is likely ascribed to the formation of diapedetic hemorrhages typical for late stages of the CT26 development [41]. It is important to note that only internal hemorrhages were examined (Fig. 3) while regions of superficial scabs forming in the later stages of tumor development, which impeded visualization of underlying vessels, were excluded from the analysis.

A decrease in the density of small- and medium-sized vessels appears to be a universal response, which was observed after irradiation in the entire dose range. For the 6 Gy and 12 Gy doses, the effect was relatively short-lived, with the return to the baseline levels observed on day 8 after irradiation. For the 18 Gy dose, the decrease in vascular density persisted for a longer period (Fig. 4A,B). At the same time, we observed a dose-independent increase in density of large hemoglobin-containing structures (Fig. 4C). Our results are in good agreement with previous reports [43] showing that small, immature vessels are most sensitive to high dose RT, with the vessels being affected proportionally to the radiation dose [6,44].

Radiation-induced changes in cervical cancer and pancreatic cancer models were studied by optical coherence angiography (OCA) revealing
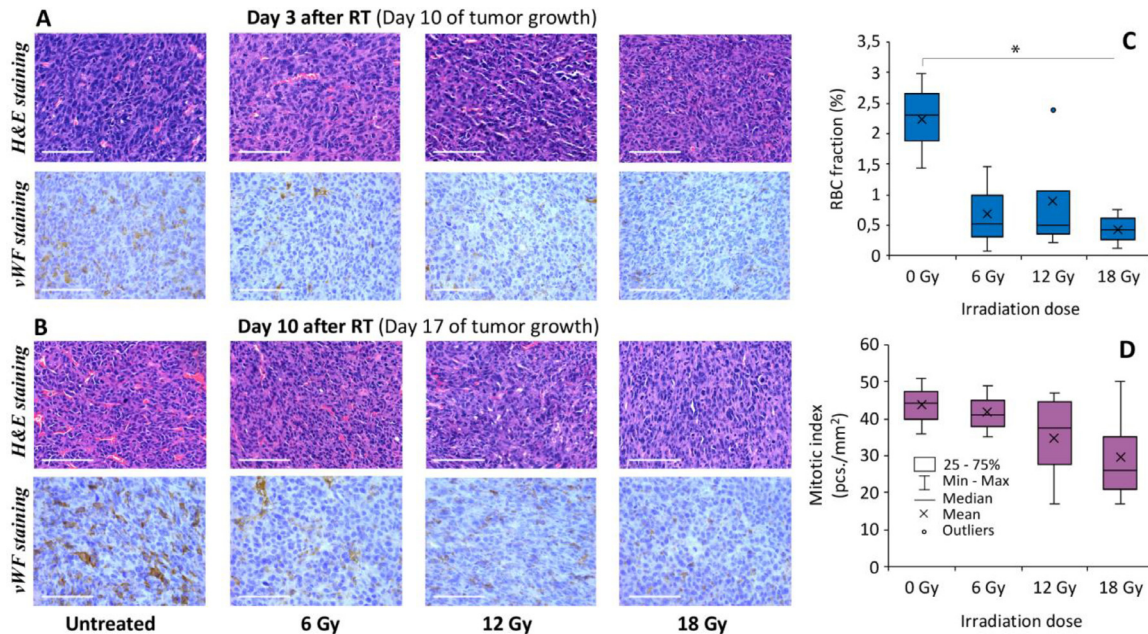
**Figure 6.** Histopathological analysis of CT26 tumors after irradiation at different doses. Examples of H&E and IHC staining with vWF antibodies in day 3 (A) and 10 (B) after irradiation; all bars are 100 μm. RBC fraction (C) and mitotic index (E) calculated from H&E-stained slides in day 10 after irradiation. * - statistically significant differences between the treatment groups.

a temporary dose-dependent drop in the vascular density [45,46]. Yet, OCA only allowed visualizing vessels with preserved blood flow, failing to depict changes in vessels where blood flow is arrested. Magnetic resonance imaging performed in the first 24 h after irradiation has previously revealed transient increase of vessel permeability, which can be attributed to tumor vessel damage [47]. A different method of microbubble-enhanced acoustic angiography was used for the long-term follow-up of rat fibrosarcoma microvasculature after irradiation [48]. The study allowed revealing the predictive value of an earlier recovery of tumor blood flow in relation to continued tumor growth.

Our results indicate that decrease in the density of small and mid-sized vessels (Fig. 4A,B) was accompanied by enhanced vessels fragmentation (Fig. 4D,E), in congruence with results obtained after irradiation of healthy tissues [20]. However, since angiogenesis is not typical for normal tissues, the alterations in the size of vascular structures were long-lasting. Our study demonstrated the significant increase in the number of vessels segments immediately after irradiation for the entire dose range. When irradiation doses were 6 Gy and 12 Gy, the number of vascular structures and their size returned to the baseline at 6 days after irradiation, arguably indicating regrowth of tumor vessels [49] (Fig. 4D,E). After the 18 Gy irradiation, sustained changes in the size and number of segments were observed until day 10 after treatment (Fig. 4F).

The increase in the number of vessels segments visualized by OA in the early post-irradiation phase may indicate an increased number of ruptured or blood-free vessels. The IHC study made it possible to discern both blood-free and damaged vessels, thus confirming this hypothesis (Fig. 6A). For the later time points, the number of small vessels was restored in the case of 6 Gy and 12 Gy irradiations, but irradiation at 18 Gy resulted in long-lasting effects. After high-dose irradiation, IHC revealed the formation of a network of very thin vessels around small clusters of tumor cells (Fig. 6B), suggesting the formation and branching of new tumor capillaries. The sizes of vascular structures were comparable to the sizes of tumor cells with some vessels represented by a single stained endothelial cell. Such small size lying below the spatial resolution limit of the OA system as well as absence of blood in the vascular lumen hindered the detection of this type of vessels in OA

images. Note that one may not rule out the influence of changes in the area of hemorrhages and the number of functional tumor vessels on the RBC fraction after radiation therapy. Since RBC fraction includes both blood vessels and hemorrhages, the analysis could instead use pairwise comparison of adjacent sections stained with eosin and a vessel marker [22].

Increase in the overall number of vessels and diminished size of small- and middle-sized vessel fragments (Figs. 4D,E and S1A,B) were accompanied by a transient increase in the size of large hemoglobin-containing structures and a drop in their number (Figs. 4F and S1C). Importantly, assessment of changes across a wide range of vascular structure dimensions has been enabled by the ultrawideband (1–100 MHz) effective detection bandwidth featured by the PVDF-based ultrasonic detector, which would not be possible with resonant-type high-frequency transducers used in conventional OA imaging systems [15].

It should be noted that due to the broad bandwidth of the detected OA responses, some blood-containing structures with borderline dimensions may appear simultaneously in more than one adjacent frequency range. In order to exclude misinterpretation of one vessel as several vessels of different diameters, more advanced volumetric image processing algorithms should be developed to accurately account for the local vessel diameter.

Radiation-induced changes of tumor vascular bed were further accompanied by dose-dependent changes of tumor oxygenation. It is important to note that, although reoxygenation is the most typical tumor response to single irradiation [50–52], the absence of radiation-induced changes or even a decrease in oxygen state have also been identified [53–56]. In our work irradiation with 6 Gy and 12 Gy doses did not lead to significant changes of $StO_2$, whereas 18 Gy dose resulted in a significant increase of $StO_2$ at 6–10 days post exposure, which is consistent with previous DOS findings [57]. DOS did not reveal a decrease in oxygenation in the first days after RT, when, according to the OA findings, the vessels were damaged. To increase the information content of the DOS measurements, oxygen saturation changes in the tumor could potentially be assessed during a gas breathing challenge, which has previously been employed for evaluating responses to vascular disrupting agents and radiation therapy [21,22,58].

Reoxygenation after RT might be caused by both enhanced tissue perfusion and drop in the oxygen consumption by dying parenchymal cells [52,53,59,60]. No significant changes in the concentration of oxyhemoglobin were detected after irradiation with the decrease in the deoxyhemoglobin concentration being the main contributor to the elevated oxygenation (Fig. S2). It can be thus concluded that the decrease in oxygenation due to vessels destruction could be compensated by the diminished oxygen consumption of irradiated cells. Late tumor reoxygenation may occur even if the presence of vascular destruction. Arguably, the inhibited cellular component plays a more significant role in the ameliorated tumor oxygenation as compared to the contribution made by the vascular alterations.

## Conclusion

Our *in vivo* imaging study revealed consistent dose- and size-dependent tumor vascular response patterns in tumors undergoing single-irradiation treatments. In the initial phases following the radiation exposure, small- and medium-sized vessels chiefly manifested a decrease in vascular density and increased vascular fragmentation accompanied by an increase in the density of large hemoglobin-containing structures. When using doses on the lower end (6 or 12 Gy), the vascular bed restores around day 6 after exposure. By contrast, when irradiated with the 18 Gy dose, the tumors responded in a prolonged fashion, with the vascular not recovering up to day 10 of the longitudinal monitoring. The absence of vessels recovery at a later stage after 18 Gy irradiation was accompanied by oxygenation impairment caused by a decrease in oxygen consumption by injured tumor cells. Importantly, the multi-scale imaging performance of OA angiography allows assessing the response of small, medium and relatively large tumor vessels simultaneously over large areas spanning several centimeters. This makes the method highly suitable for microangiographic observations on the whole tumor scale with the main limitation being the inability to visualize capillaries smaller than 15 $\mu$m in diameter as well as vessels containing no erythrocytes.

### Declaration of Competing Interest

The authors have declared that no competing interest exists

## CRediT authorship contribution statement

**Anna Orlova:** Conceptualization, Funding acquisition, Supervision, Methodology, Formal analysis, Writing – original draft. **Ksenia Pavlova:** Methodology, Formal analysis, Writing – original draft. **Aleksey Kurnikov:** Methodology, Software, Formal analysis. **Anna Maslennikova:** Conceptualization, Methodology, Writing – review & editing. **Marina Myagcheva:** Methodology, Formal analysis, Writing – review & editing. **Evgeniy Zakharov:** Methodology, Formal analysis, Writing – review & editing. **Dmitry Skamnitskiy:** Methodology. **Valeria Perekatova:** Software. **Alexander Khilov:** Software. **Andrey Kovalchuk:** Software. **Alexander Moiseev:** Formal analysis. **Ilya Turchin:** Writing – review & editing. **Daniel Razansky:** Funding acquisition, Supervision, Formal analysis, Writing – review & editing. **Pavel Subochev:** Conceptualization, Funding acquisition, Supervision, Software, Methodology, Formal analysis, Writing – review & editing.

## Funding

## Acknowledgements

## Supplementary materials

Supplementary material associated with this article can be found, in the online version, at doi:10.1016/j.neo.2022.100778.

## References

[1] Park HJ, Griffin RJ, Hui S, Levitt SH, Song CW. Radiation-induced vascular damage in tumors: implications of vascular damage in ablative hypofractionated radiotherapy (SBRT and SRS). *Radiat. Res.* 2012;**177**:311–27.

[2] Goedegebuure RS, de Klerk LK, Bass AJ, Derks S, Thijssen VL. Combining radiotherapy with anti-angiogenic therapy and immunotherapy; a therapeutic triad for cancer? *Front. Immunol.* 2019;**9**:3107.

[3] Arnold KM, Flynn NJ, Raben A, Romak L, Yu Y, Dicker AP, Mourtada F, Sims-Mourtada J. The impact of radiation on the tumor microenvironment: effect of dose and fractionation schedules. *Cancer Growth Metastasis* 2018;**11**:1179064418761639.

[4] Barker HE, Paget JT, Khan AA, Harrington KJ. The tumour microenvironment after radiotherapy: mechanisms of resistance and recurrence. *Nat. Rev. Cancer* 2015;**15**:409–25.

[5] Song CW, Park I, Cho LC, Yuan J, Dusenbery KE, Griffin RJ, Levitt SH. Is indirect cell death involved in response of tumors to stereotactic radiosurgery and stereotactic body radiation therapy. *Int. J. Radiat. Oncol. Biol. Phys.* 2014;**89**:924–5.

[6] Kolesnick R, Fuks Z. Radiation and ceramide-induced apoptosis. *Oncogene* 2003;**22**:5897–906.

[7] Schambach SJ, Bag S, Schilling L, Groden C, Brockmann MA. Application of micro-CT in small animal imaging. *Methods* 2010;**50**:2–13.

[8] Johnson GA, Cofer GP, Gewalt SL, Hedlund LW. Morphologic phenotyping with MR microscopy: the visible mouse. *Radiology* 2002;**222**:789–93.

[9] Gigan S. Optical microscopy aims deep. *Nat. Photonics* 2017;**11**:14–16.

[10] Matveev LA, Zaitsev VY, Gelikonov GV, Matveyev AL, Moiseev AA, Ksenofontov SY, Gelikonov VM, Sirotkina MA, Gladkova ND, Demidov V. Hybrid M-mode-like OCT imaging of three-dimensional microvasculature *in vivo* using reference-free processing of complex valued B-scans. *Opt. Lett.* 2015;**40**:1472–5.

[11] Orlova AG, Subochev PV, Moiseev AA, Smolina E, Ksenofontov SY, Kirillin MY, Shakhova NM. Bimodal imaging of functional changes in blood flow using optoacoustic and optical coherent angiography. *Quantum Electron.* 2019;**49**:25.

[12] Hwang JY. Doppler ultrasonography of the lower extremity arteries: anatomy and scanning guidelines. *Ultrasonography* 2017;**36**:111.

[13] Kumagai K, Koike H, Nagaoka R, Sakai S, Kobayashi K, Saijo Y. High-resolution ultrasound imaging of human skin *in vivo* by using three-dimensional ultrasound microscopy. *Ultrasound Med. Biol.* 2012;**38**:1833–8.

[14] Deán-Ben X, Gottschalk S, Mc Larney B, Shoham S, Razansky D. Advanced optoacoustic methods for multiscale imaging of in vivo dynamics. *Chem. Soc. Rev.* 2017;**46**:2158–98.

[15] Haedicke K, Agemy L, Omar M, Berezhnoi A, Roberts S, Longo-Machado C, Skubal M, Nagar K, Hsu HT, Kim K. High-resolution optoacoustic imaging of tissue responses to vascular-targeted therapies. *Nat. Biomed. Eng.* 2020;**4**:286–97.

[16] Zhou HC, Chen N, Zhao H, Yin T, Zhang J, Zheng W, Song L, Liu C, Zheng R. Optical-resolution photoacoustic microscopy for monitoring vascular normalization during anti-angiogenic therapy. *Photoacoustics* 2019;**15**:100143.

[17] Rich LJ, Seshadri M. Photoacoustic monitoring of tumor and normal tissue response to radiation. *Sci. Rep.* 2016;**6**:1–10.

[18] Rich LJ, Miller A, Singh AK, Seshadri M. Photoacoustic imaging as an early biomarker of radio therapeutic efficacy in head and neck cancer. *Theranostics* 2018;**8**:2064.

[19] Hysi E, Fadhel MN, Wang Y, Sebastian JA, Giles A, Czarnota GJ, Exner AA, Kolios MC. Photoacoustic imaging biomarkers for monitoring biophysical changes during nanobubble-mediated radiation treatment. *Photoacoustics* 2020;**20**:100201.

[20] Estrada H, Rebling J, Sievert W, Hladik D, Hofmann U, Gottschalk S, Tapio S, Multhoff G, Razansky D. Intravital optoacoustic and ultrasound bio-microscopy reveal radiation-inhibited skull angiogenesis. *Bone* 2020;**133**:115251.

[21] Guo Y, Wang H, Gerberich JL, Odutola SO, Charlton-Sevcik AK, Li M, Tanpure RP, Tidmore JK, Trawick ML, Pinney KG. Imaging-guided evaluation of the novel small-molecule benzosuberene tubulin-binding agent KGP265 as a potential therapeutic agent for cancer treatment. *Cancers* 2021;**13**:4769.

[22] Tomaszewski MR, Gehrung M, Joseph J, Quiros-Gonzalez I, Disselhorst JA, Bohndiek SE. Oxygen-enhanced and dynamic contrast-enhanced optoacoustic tomography provide surrogate biomarkers of tumor vascular function, hypoxia, and necrosis. *Cancer Res.* 2018;**78**:5980–91.

[23] Johnson SP, Ogunlade O, Lythgoe MF, Beard P, Pedley RB. Longitudinal photoacoustic imaging of the pharmacodynamic effect of vascular targeted therapy on tumors. *Clin. Cancer Res.* 2019;**25**:7436–47.

[24] Subochev PV, Prudnikov M, Vorobyev V, Postnikova AS, Sergeev E, Perekatova VV, Orlova AG, Kotomina V, Turchin IV. Wideband linear detector arrays for optoacoustic imaging based on polyvinylidene difluoride films. *J. Biomed. Opt.* 2018;**23**:091408.

[25] Subochev P, Smolina E, Sergeeva E, Kirillin M, Orlova A, Kurakina D, Emyanov D, Razansky D. Toward whole-brain *in vivo* optoacoustic angiography of rodents: modeling and experimental observations. *Biomedical optics express* 2020;**11**:1477–88.

[26] Subochev P. Cost-effective imaging of optoacoustic pressure, ultrasonic scattering, and optical diffuse reflectance with improved resolution and speed. *Opt. Lett.* 2016;**41**:1006–9.

[27] Subochev P, Orlova A, Mikhailova I, Shilyagina N, Turchin I. Simultaneous *in vivo* imaging of diffuse optical reflectance, optoacoustic pressure, and ultrasonic scattering. *Biomed. Opt. Express* 2016;**7**:3951–7.

[28] Jaeger M, Schüpbach S, Gertsch A, Kitz M, Frenz M. Fourier reconstruction in optoacoustic imaging using truncated regularized inverse k-space interpolation. *Inverse Prob.* 2007;**23**:S51.

[29] Kurnikov A, Pavlova K, Orlova AG, Khilov AV, Perekatova V, Kovalchuk A, Subochev PV. Broadband (100 kHz–100 MHz) ultrasound PVDF detectors for raster-scan optoacoustic angiography with acoustic resolution. *Quantum Electron.* 2021;**51**:383.

[30] Moore MJ, Hysi E, Fadhel MN, El-Rass S, Xiao Y, Wen XY, Kolios MC. Photoacoustic F-mode imaging for scale specific contrast in biological systems. *Commun. Phys.* 2019;**2**:1–10.

[31] Kleshnin MS, IyV T. Evaluation of oxygenation in the surface layers of biological tissues based on diffuse optical spectroscopy with automated calibration of measurements. *Quantum Electron.* 2019;**49**:628.

[32] Kleshnin MS. Deep learning neural network estimation of tissue oxygenation based on diffuse optical spectroscopy. *Laser Phys.* 2019;**29**:085603.

[33] Calabro K, Curtis A, Galarneau JR, Krucker T, Bigio IJ. Gender variations in the optical properties of skin in murine animal models. *J. Biomed. Opt.* 2011;**16**:011008.

[34] Sabino CP, Deana AM, Yoshimura TM, da Silva DF, França CM, Hamblin MR, Ribeiro MS. The optical properties of mouse skin in the visible and near infrared spectral regions. *J. Photochem. Photobiol. B* 2016;**160**:72–8.

[35] Hather G, Liu R, Bandi S, Mettetal J, Manfredi M, Shyu WC, Donelan J, Chakravarty A. Growth rate analysis and efficient experimental design for tumor xenograft studies: supplementary issue: array platform modeling and analysis (A). *Cancer Inform.* 2014;**13**:S13974 CIN.

[36] Greening GJ, Miller KP, Spainhour CR, Cato MD, Muldoon TJ. Effects of isoflurane anesthesia on physiological parameters in murine subcutaneous tumor

[37] allografts measured via diffuse reflectance spectroscopy. *Biomed. Opt. Express* 2018;**9**:2871–86.

Greening G, Mundo A, Rajaram N, Muldoon TJ. Sampling depth of a diffuse reflectance spectroscopy probe for *in-vivo* physiological quantification of murine subcutaneous tumor allografts. *J. Biomed. Opt.* 2018;**23**:085006.

[38] Forster JC, Harriss-Phillips WM, Douglass MJ, Bezak E. A review of the development of tumor vasculature and its effects on the tumor microenvironment. *Hypoxia* 2017;**5**:21.

[39] Volz J, Mammadova-Bach E, Gil-Pulido J, Nandigama R, Remer K, Sorokin L, Zernecke A, Abrams SI, Ergün S, Henke E. Inhibition of platelet GPVI induces intratumor hemorrhage and increases efficacy of chemotherapy in mice. *Blood J. Am. Soc. Hematol.* 2019;**133**:2696–706.

[40] Orlova A, Sirotkina M, Smolina E, Elagin V, Kovalchuk A, Turchin I, Subochev P. Raster-scan optoacoustic angiography of blood vessel development in colon cancer models. *Photoacoustics* 2019;**13**:25–32.

41 Kuznetsov S, Snopova L, Karabut M, Sirotkina M, Buyanova N, Kalganova T, Elagin V, Senina-Volzhskaya I, Barbashova L, Shumilova A. Features of morphological changes in experimental CT-26 tumors growth. *Mod. Technol. Med.* 2015;**7**:32–9.

[42] Seguin J, Doan BT, Latorre Ossa H, Jugé L, Gennisson JL, Tanter M, Scherman D, Chabot GG, Mignet N. Evaluation of nonradiative clinical imaging techniques for the longitudinal assessment of tumour growth in murine CT26 colon carcinoma. *Int. J. Mol. Imaging* 2013;**2013**.

[43] Jani A, Shaikh F, Barton S, Willis C, Banerjee D, Mitchell J, Hernandez SL, Hei T, Kadenhe-Chiweshe A, Yamashiro DJ. High-dose, single-fraction irradiation rapidly reduces tumor vasculature and perfusion in a xenograft model of neuroblastoma. *Int. J. Radiat. Oncol. Biol. Phys.* 2016;**94**:1173–80.

[44] Baker DG, Krochak RJ. The response of the microvascular system to radiation: a review. *Cancer Invest.* 1989;**7**:287–94.

[45] Maeda A, Leung MK, Conroy L, Chen Y, Bu J, Lindsay PE, Mintzberg S, Virtanen C, Tsao J, Winegarden NA. *In vivo* optical imaging of tumor and microvascular response to ionizing radiation. *PLoS One* 2012;**7**: e42133.

[46] Demidov V, Maeda A, Sugita M, Madge V, Sadanand S, Flueraru C, Vitkin IA. Preclinical longitudinal imaging of tumor microvascular radiobiological response with functional optical coherence tomography. *Sci. Rep.* 2018;**8**:1–12.

[47] Brown SL, Nagaraja TN, Aryal MP, Panda S, Cabral G, Keenan KA, Elmghirbi R, Mikkelsen T, Hearshen D, Knight RA. MRI-tracked tumor vascular changes in the hours after single-fraction irradiation. *Radiat. Res.* 2015;**183**:713–21.

[48] Kasoji SK, Rivera JN, Gessner RC, Chang SX, Dayton PA. Early assessment of tumor response to radiation therapy using high-resolution quantitative microvascular ultrasound imaging. *Theranostics* 2018;**8**:156.

[49] Clément-Colmou K, Potiron V, Pietri M, Guillonneau M, Jouglar E, Chiavassa S, Delpon G, Paris F, Supiot S. Influence of radiotherapy fractionation schedule on the tumor vascular microenvironment in prostate and lung cancer models. *Cancers* 2020;**12**:121.

[50] Koutcher JA, Alfieri AA, Devitt ML, Rhee JG, Kornblith AB, Mahmood U, Merchant TE, Cowburn D. Quantitative changes in tumor metabolism, partial pressure of oxygen, and radiobiological oxygenation status postradiation. *Cancer Res.* 1992;**52**:4620–7.

[51] Fujii H, Sakata KI, Katsumata Y, Sato R, Kinouchi M, Someya M, Masunaga S-i, Hareyama M, Swartz HM, Hirata H. Tissue oxygenation in a murine SCC VII tumor after X-ray irradiation as determined by EPR spectroscopy. *Radiother. Oncol.* 2008;**86**:354–60.

[52] Orlova A, Maslennikova A, Golubiatnikov GY, Suryakova A, Kirillin MY, Kurakina D, Kalganova T, Volovetsky A, Turchin I. Diffuse optical spectroscopy assessment of rodent tumor model oxygen state after single-dose irradiation. *Biomed. Phys. Eng. Express* 2019;**5**:035010.

[53] Fenton BM, Lord EM, Paoni SF. Effects of radiation on tumor intravascular oxygenation, vascular configuration, development of hypoxia, and clonogenic survival. *Radiat. Res.* 2001;**155**:360–8.

[54] Zhou H, Zhang Z, Denney R, Williams JS, Gerberich J, Stojadinovic S, Saha D, Shelton JM, Mason RP. Tumor physiological changes during hypofractionated

stereotactic body radiation therapy assessed using multi-parametric magnetic resonance imaging. *Oncotarget* 2017;**8**:37464.

[55] O'Hara JA, Goda F, Demidenko E, Swartz HM. Effect on regrowth delay in a murine tumor of scheduling split-dose irradiation based on direct measurements by electron paramagnetic resonance oximetry. *Radiat. Res.* 1998;**150**:549–56.

[56] Sunar U, Makonnen S, Zhou C, Durduran T, Yu G, Wang HW, Lee WM, Yodh AG. Hemodynamic responses to antivascular therapy and ionizing radiation assessed by diffuse optical spectroscopies. *Opt. Express* 2007;**15**:15507–16.

[57] Vishwanath K, Klein DH, Chang K, Schroeder T, Dewhirst MW, Ramanujam N. Quantitative optical spectroscopy can identify long-term local tumor control in irradiated murine head and neck xenografts. *J. Biomed. Opt.* 2009;**14**:054051.

[58] Arai TJ, Yang DM, Campbell JW, Tsuicheng C, Cheng X, Stojadinovic S, Peschke P, Mason RP. Oxygen-sensitive MRI: a predictive imaging biomarker for tumor radiation response? *Int. J. Radiat. Oncol. Biol. Phys.* 2021;**110**:1519–29.

[59] Wachsberger P, Burd R, Dicker AP. Tumor response to ionizing radiation combined with antiangiogenesis or vascular targeting agents: exploring mechanisms of interaction. *Clin. Cancer Res.* 2003;**9**:1957–71.

[60] Bussink J, Kaanders JHA, Rijken PFJ, Raleigh JA, Van der Kogel AJ. Changes in blood perfusion and hypoxia after irradiation of a human squamous cell carcinoma xenograft tumor line. *Radiat. Res.* 2000;**153**:398–404.